Imperfect supercritical bifurcation in a three-dimensional turbulent wake

Olivier Cadot and Antoine Evrard
IMSIA-ENSTA ParisTech, CNRS, CEA, EDF, Université Paris-Saclay, 91762 Palaiseau cedex, France

Luc Pastur
LIMSI-Univ Paris Sud, CNRS, Université Paris-Saclay, 91403 Orsay cedex, France
(Received 9 February 2015; revised manuscript received 15 April 2015; published 12 June 2015)

The turbulent wake of a square-back body exhibits a strong bimodal behavior. The wake randomly undergoes symmetry-breaking reversals between two mirror asymmetric steady modes [reflectional symmetry-breaking (RSB) modes]. The characteristic time for reversals is about 2 or 3 orders of magnitude larger than the natural time for vortex shedding. Studying the effects of the proximity of a ground wall together with the Reynolds number, it is shown that the bimodal behavior is the result of an imperfect pitchfork bifurcation. The RSB modes correspond to the two stable bifurcated branches resulting from an instability of the stable symmetric wake. An attempt to stabilize the unstable symmetric wake is investigated using a passive control technique. Although the controlled wake still exhibits strong fluctuations, the bimodal behavior is suppressed and the drag reduced. This promising experiment indicates the possible existence of an unstable solution branch corresponding to a reflectional symmetry preserved (RSP) mode. This work is encouraging to develop a control strategy based on a stabilization of this RSP mode to reduce mean drag and lateral force fluctuations.

DOI: 10.1103/PhysRevE.91.063005 PACS number(s): 47.20.Ky, 47.15.Fe, 47.27.Cn, 47.27.wb

I. INTRODUCTION

In the Navier-Stokes equations, symmetry breaking and bifurcations are the key ingredients for the laminar-to-turbulent transition. They appear in the flow solutions as the control parameter (i.e., the Reynolds number) is increased. Normally, the strongest modifications in the flow appear during the lowest part of the transitional range of Reynolds numbers. The highest part of the transitional range is reached when all the symmetries are restored in the statistical sense [1]. However, there are some cases for which such high Reynolds number flows may undergo large-scale symmetry breaking.

One of the most spectacular occurs during the drag crisis transitions of smooth bluff bodies [2]. In the critical Reynolds number regime of a circular cylinder ($10^5 < \mathrm{Re} < 5 \times 10^5$), the laminar-to-turbulent transition of the free boundary layers is accompanied by the occurrence of asymmetric wake flow states [3,4] producing a nonzero mean lift. They are commonly called one bubble and two bubbles transitions corresponding, respectively, to the reattachment on one side and both sides of the cylinder. From global force [5,6] and local pressure [7] measurements, the existence of bistable behaviors in this critical range has been evidenced through hysteretic discontinuities in the Strouhal-Reynolds number relationship. Schewe [5] associated each discontinuity with a subcritical bifurcation during which the energy of the force fluctuations is dominated by the contribution of a wide low-frequency domain [5–7]. This domain belongs to lower frequencies than the nearly extinguished frequencies of the Kármán global modes. Recently, the examination of pressure time series measured on the cylinder [8,9] revealed that reattachments might switch from one side to the other unpredictably in time during the drag crisis fluctuations. Further analyses by Cadot *et al.* [10] confirmed that the strong fluctuations were the consequence of the random exploration of few identified asymmetric and symmetric metastable states.

Another case of large-scale symmetry breaking was studied more recently in a totally different flow configuration [11–15]; the von Kármán swirling flow geometry. It is basically a closed turbulent flow forced between two counter-rotating stirrers facing each other in a cylindrical tank. The transition that occurs around $\mathrm{Re} = 10^4$ consists of a bifurcation of the basic symmetric flow topology toward two other flow topologies which break the symmetry of the driving geometry [11,13]. In Refs. [12,14,15], random switching between two metastable symmetry-breaking states are observed. In that case, the symmetry is restored in a statistical sense, but a state remains observable over durations much larger than the time scale of the turbulence large scale. Another difference with the drag crisis case is that the symmetry-breaking modes in the von Kármán swirling flow geometry are also observable in the laminar regime during the transition scenario to turbulence [16,17] and the symmetry breaking in the turbulent regime might be reminiscent of these modes.

Even more recently, the three-dimensional wake of a generic square-back body has been shown to switch randomly between two asymmetric metastable states over a wide range of Reynolds numbers from 300 to 10^7 [18–20]. Their observation in the laminar regime [18] excludes the possibility of an origin associated with turbulent boundary layer reattachment as for those present during the drag crisis transition. The authors referred to this as a bistable behavior of the wake, unpredictable in time with a long-time dynamics, 2 or 3 orders of magnitude larger than the time dynamics for vortex shedding. The metastable states break the reflectional symmetry of the setup and will be referred to in the following as reflectional symmetry-breaking (RSB) modes. On the theoretical background, RSB modes of three-dimensional wakes are actually known to be bifurcated states of the basic symmetric state observed in the laminar regime (see the stability analysis of Pier [21] for a sphere or a disk and, very recently, Marquet and Larsson [22] for rectangular plates of different aspect ratio). In the work of Grandemange *et al.* [20], the bistability was found to be inhibited when the body was approaching the ground wall at a Reynolds number of 4.5×10^4, leading to a high-Reynolds-number transition.

The present work aims at characterizing this transition in the turbulent wake using independently two control parameters: the ground clearance C (distance from the ground wall to the body) and the Reynolds number Re. A global quantity giving a topological indicator of the wake will be used as the order parameter of the transition. The questions we would like to address are as follows: Does the turbulent wake flow have an unstable symmetric solution when it explores randomly the metastable RSB modes? The answer might have relevant applications for flow control strategies at industrial scale (i.e., large Reynolds number flow). Second, from a more general perspective, what are the similarities between this transition and those of the von Kármán swirling flow geometry?

The article is organized as follows. Section II is in two parts and describes the geometry and the measurements. Section III is presented in five parts. Section III A defines and characterizes the global quantity that is used as the order parameter to describe the transition. Section III B shows that the transition does not depend on the yaw angle of the body. Section III C shows the existence of a pitchfork bifurcation and sets the phase diagram of the bifurcation versus ground clearance and Reynolds number. In Sec. III D we attempt to stabilize the turbulent symmetric wake flow and Sec. III E illustrates the main result with some flow visualizations in a water tunnel at a comparable Reynolds number. Finally, conclusive remarks end the paper in Sec. IV.

II. EXPERIMENTAL SETUP

A. Geometry and measurements

The experimental setup is illustrated in Fig. 1. A ground plate is placed in an Eiffel-type wind tunnel having a turbulent intensity less than 0.3%. The homogeneity of the velocity over the 390 mm × 400 mm section is 0.4%. The wake is generated by the square-back geometry first used in the experiments of Ref. [23] as a simplified model to study ground vehicle aerodynamics. The total length of the body is $L = 261.0$ mm, and the height H and width W of the base are, respectively, 72.0 and 97.2 mm. The four supports are cylindrical with a diameter of 7.5 mm. The blockage ratio is less than 5%. The coordinate system is defined as x in the streamwise direction, z is normal to the ground, and y forms a direct trihedral. The Reynolds number of the flow is defined as $\mathrm{Re} = U_0 H/\nu$, where U_0 is the uniform flow velocity ranging from 3.7 m s^{-1} to 33 m s^{-1} and ν the air kinematic viscosity. The explored range of Reynolds numbers is thus comprised within 1.7×10^4 to 1.6×10^5.

The body is fixed on a turntable to allow side slip conditions with a yaw angle β [see Fig. 1(b)]. The rotation mechanism is driven by a displacement controlled by a Newport Motion Controller ESP301; the precision of the robot is better than 0.02°. Another displacement also controlled by the ESP301 allows adjustment of the ground clearance in the range $0 < C < 12.5$ mm. The precision is better than 10 μm. In the following experiments, the ground clearance is increased in steps of 250 μm.

The pressure on the body is measured at 21 locations at the body base [see blue dots in Fig. 1(c)]. The taps are distributed symmetrically referring to the planes $y = 0$ and $z = 0$, the latter plane corresponding to the midheight of the geometry. The pressure is obtained using a ZOC22 pressure scanner and a GLE/SmartZOC-100 electronic for data acquisition using an ethernet connection to the PC. The high cut-off frequency of each transducer is larger than 250 Hz. It is acquired at a sample rate of 500 Hz per channel, with an accuracy of ±3.75 Pa. The pressure scanner is located inside the model; it is denoted "P scan" in Figs. 1(a) and 1(b). It is linked to each tap with less than 100 mm of vinyl tubes to limit the filtering effect of the tubing. In that case, the high cut-off frequency falls to 150 Hz. This device is connected to the electronic GLE/SmartZOC-100 using a connection cable going through one of the four cylindrical supports of the model so, apart from these supports, nothing disturbs the underbody flow. The pressure coefficient is calculated as follows:

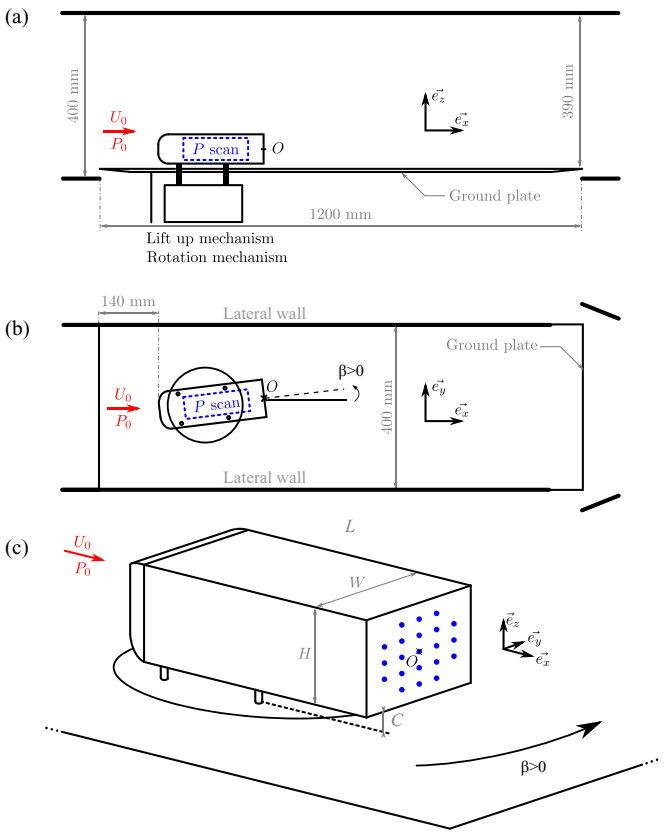

FIG. 1. (Color online) Experimental setup. Side view (a), top view (b), and perspective view (c); the point O at the center of the body base sets the origin of the coordinate system. The blue dots locate the visible pressure taps; P scan refers to the pressure scanner.

$$C_p = \frac{p - p_0}{\frac{1}{2}\rho U_0^2}, \tag{1}$$

where p_0 is the static pressure in the tunnel just before the test section and the dynamic pressure $\frac{1}{2}\rho U_0^2$ is measured from a Pitot tube at the entrance of the test section.

In the following, the use of an asterisk for a^* denotes the nondimensional value of any quantity $a(x,y,z,t)$ made dimensionless by a combination of the height H and the inlet velocity U_0.

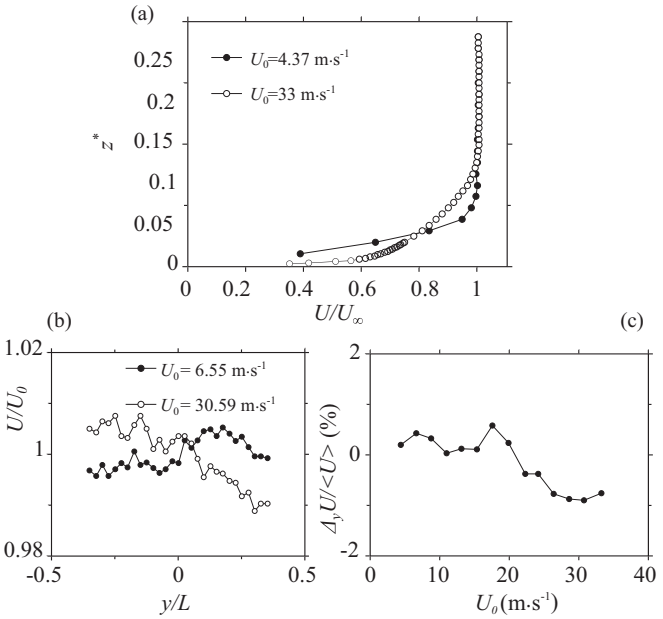

FIG. 2. Free stream characterization at the location of the Ahmed body, boundary layer profile on the floor (a), lateral velocity profile at $z^* = 1/2$ (b), right-to-left asymmetry (see text) of the lateral velocity profile vs the main velocity (c).

B. Free stream characterization

In order to control the constant flow conditions, the ground plate (floor) is placed at 10 mm above the bottom side of the inlet [see Fig. 1(a)] and triggers the boundary layer at its leading edge, without any separation, 140 mm upstream of the fore-body. The boundary layer on the floor of the free stream at the body location (say $X = 260$ mm from the leading edge of the ground plate and without the body) is shown in Fig. 2 for the two extreme main flow velocities of the explored range. The boundary layer profile at the lowest velocity has a Reynolds number based on the development length $\mathrm{Re}_X = 0.75 \times 10^5$ and suggests that it is laminar at the lowest velocity. At the largest velocity, $\mathrm{Re}_X = 5.72 \times 10^5$ and the shape suggests a turbulent boundary layer. For both cases, the thickness never exceeds $\delta^*_{0.99} = 0.1$. The laminar-turbulent transition occurs around 14 m s^{-1}, say, $\mathrm{Re}_X = 2.42 \times 10^5$. However, this transition has no meaning considering the flow around the Ahmed body whose presence produces pressure gradients at the ground wall that modifies drastically the boundary layer history compared to a development on the flat floor alone.

The spanwise spatial homogeneity is characterized through the velocity measurements in Fig. 2(b). Although the spatial inhomogeneity still remains below 0.4% in rms quantities, the streamwise velocity displays a small but significant shear whose sign depends upon the mean flow velocity. Figure 2(c) shows the difference between the mean velocity computed from the right-hand side of the tunnel ($y > 0$) and the left-hand side of the tunnel ($y < 0$). There is a velocity excess on the left-hand side of the free stream of about 1% for mean flow velocities larger than 20 m s^{-1}. These symmetrical defects in the free stream have to be acknowledged considering their induced bias in the onset of a symmetry-breaking instability.

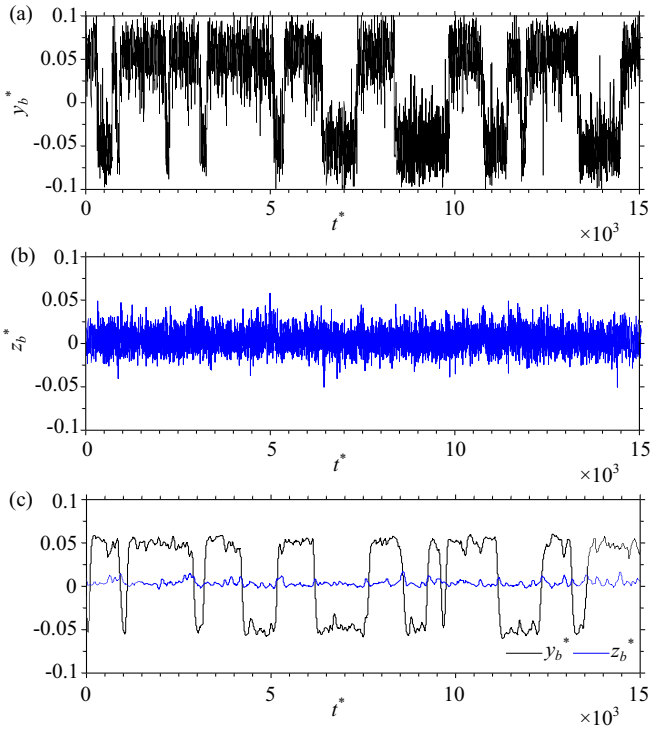

FIG. 3. (Color online) Time series of the base pressure barycenter coordinates (y_b^*, z_b^*), y_b^* (a), z_b^* (b), and filtered in (c).

III. RESULTS

A. Global quantities for the near wake

The pressure distribution at the base of the body has been shown to be a relevant indicator [19,20,24,25] of the large-scale wake topology. As in Ref. [25], we will use the instantaneous barycenter of the base pressure distribution, which we define as:

$$\vec{r}_b(y_b, z_b) = \frac{\iint_{\mathrm{Base}} \vec{r} C_p(\vec{r}) dy dz}{\iint_{\mathrm{Base}} C_p(\vec{r}) dy dz}, \tag{2}$$

It should be noted that for a massively separated wake flow as in the present case, the pressure of the base is always lower than the static pressure of the free stream, meaning that the denominator in Eq. (2) is nonzero and always negative. Figures 3(a) and 3(b) shows the two components of the base pressure barycenter. Its horizontal component in Fig. 3(a) clearly exhibits the bimodal behavior. The two most probable horizontal positions observed at $y_b^* \simeq \pm 0.05$ are associated with the two deflected wakes fully characterized in Ref. [19]. They correspond to the two mirror RSB modes breaking the reflectional symmetry with respect of the plane $y = 0$ of the setup. As already been shown in Ref. [19] the characteristic time scale to switch between these modes is 2 to 3 orders of magnitude larger than the natural time scale $T^* = 1$ in nondimensional units (i.e., $T = \frac{H}{U_0}$). For the remainder of this study, time series are low-pass filtered to focus on this long-time dynamics, with a cut-off frequency $f_c^* = \frac{1}{250}$ (say $f_c = 0.22$ Hz at $U_0 = 4$ m s^{-1} to $f_c = 1.83$ Hz at $U_0 = 33$ m s^{-1}). The filtered data are shown for the barycenter coordinates in Fig. 3(c).

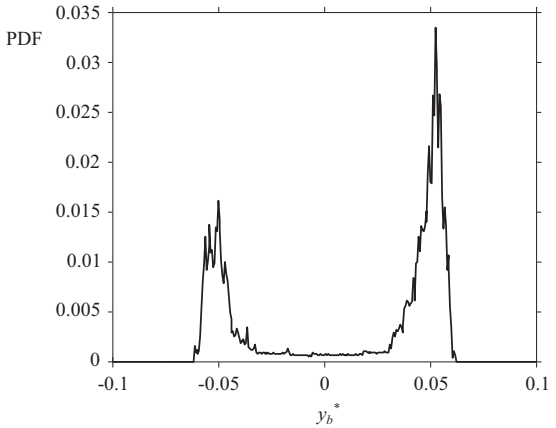

FIG. 4. Probability density function (PDF) of the horizontal coordinate y_b^* of the base pressure barycenter computed from the time series in Fig. 3(c).

The most probable positions of the pressure barycenter are extracted from probability density functions (PDFs) such as the one presented in Fig. 4. The statistics are performed over a duration fixed to 50 s ($\tau^* = 27\,500$ at $U_0 = 33$ m s^{-1} and $\tau^* = 3300$ at $U_0 = 4$ m s^{-1}). The choice of recording duration is a compromise between an accurate estimation of the position of the most probable events and the high cost of time due to a parametric study involving changes in yaw angle, ground clearance, and Reynolds number. As we can attest from Fig. 4, the most probable event positions are sufficiently well defined to investigate the parametric study of the stable branch solutions. Note that the chosen recording time that evolves in the range $\tau^* \sim 3000-27\,500$ leads unavoidably to weakly converged PDFs because of the long-time dynamics associated with the RSB modes having a characteristic time scale in the range $\tau^* \sim 100-1000$ [19]. Hence, the weak convergence does not allow an accurate estimate of the value of the corresponding probability density.

Another global quantity of interest is the base suction $-C_{pb}$, where:

$$C_{pb} = \frac{1}{S}\iint_{\text{Base}} C_p(\vec{r})dydz. \tag{3}$$

The base suction is directly related to the form drag (see Refs. [26,27] and references therein), whereby the larger the base suction the larger the form drag. Note that the discrete pressure taps distribution at the base [Fig. 1(c)] will not lead to an exact measurement of the base suction but rather to a drag indicator.

B. Wake mode sensitivity to a yaw angle β and ground clearance C^*

Figure 5 shows the PDFs of the statistical variable y_b^*, for 10 sets of experiments performed for the same Reynolds number Re = 146 800. The gray levels of the PDFs allow the most probable positions of the barycenter, which contains the main information, to be located. For each set, the ground clearance C^* is fixed and the yaw angle is varied within the range $-1^\circ < \beta < +1^\circ$ in step of 0.1°. By looking at the PDFs at the top of Fig. 5 obtained for the ground clearance $C^* = 0.153$,

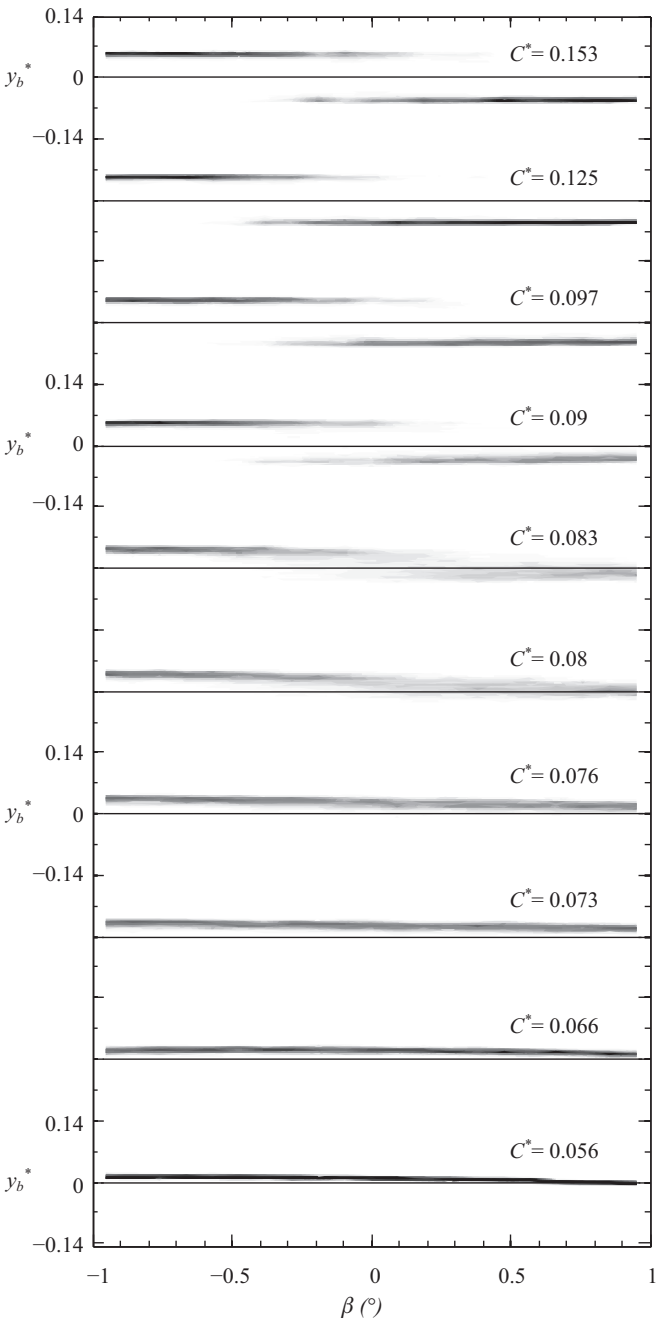

FIG. 5. Evolution of the probability density function, PDF(y_b^*), in gray levels (the darker, the larger the PDF) for $U_0 = 30.58$ m s^{-1} with the yaw angle β and for different ground clearances C^*.

we notice that two distinguished most probable positions, symmetrically located at $y_b^{*+} \simeq 0.05$ and $y_b^{*-} \simeq -0.05$, are observable. These two positions are associated with the two stable mirror states and the values of $y_b^{*\pm}$ do not depend on the yaw angle. When the ground clearance is decreased to $C^* = 0.09$, similar observations can be made except that now the two positions are not symmetrically located anymore. It emphasizes the sensitivity to symmetry defects in the setup, especially related to the nonuniformity of the incoming flow as described in Fig. 2.

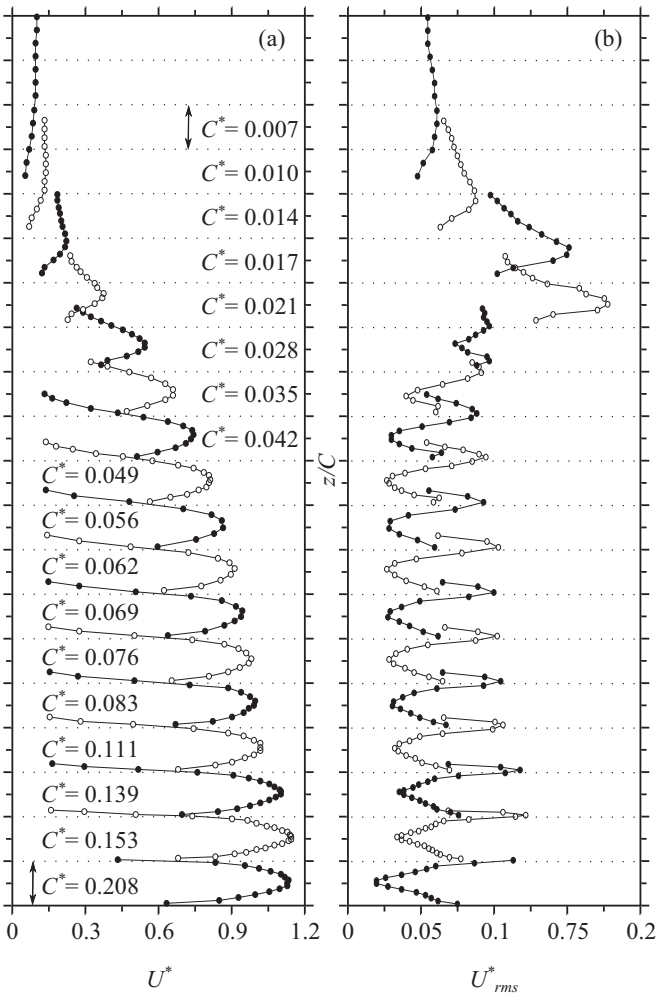

FIG. 6. Characterization of the underbody flow using hot wire anemometer measurements, 2 mm behind the body in the $y = 0$ plane. The hot wire is oriented to be sensitive to the longitudinal velocity $u(t)$. (a) z/C vs the time averaged nondimensional velocity $U^* = \overline{u^*}$. (b) Fluctuating velocity defined as $U^*_{\rm rms} = \sqrt{\overline{(u^* - U^*)^2}}$.

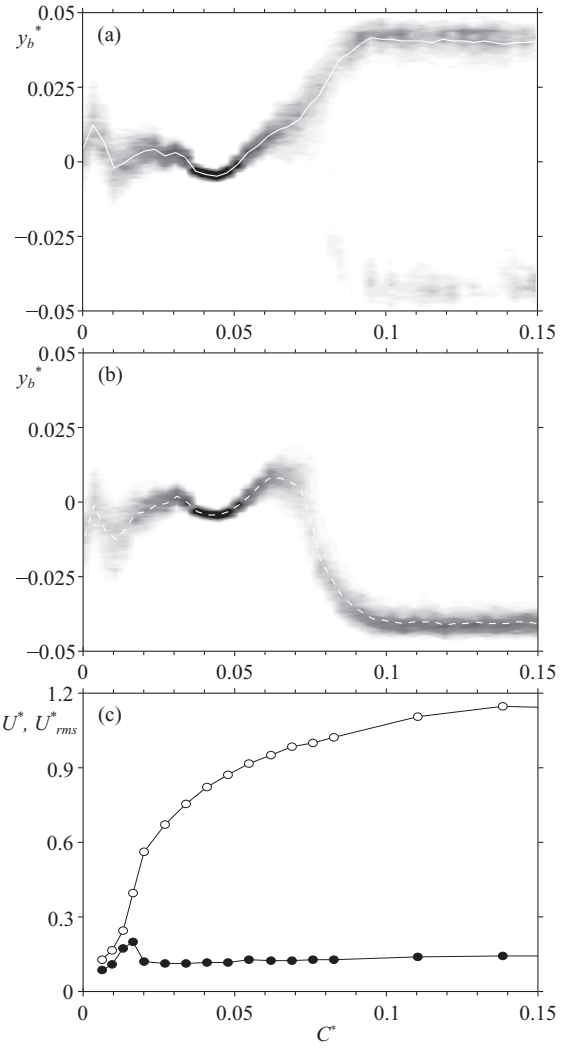

FIG. 7. Probability density functions, PDF(y^*_b) in gray levels for $U_0 = 30.58\ {\rm m\,s^{-1}}$ vs the ground clearance C^*, for (a) with the yaw angle $\beta = -0.4^\circ$ and (b) with a yaw angle $\beta = +0.4^\circ$. The white lines represent the most probable position and correspond in [(a), continuous line] to the stable branch y^{*+}_b and in [(b), dashed line] to the other stable branch y^{*-}_b. In (c) are reported the maximum of the profiles measured in Fig. 6, mean velocity U^* (empty circles) and fluctuation $U^*_{\rm rms}$ (black filled circles).

For slightly smaller C^*, the two states become hardly distinguishable and, instead, a continuous change in the pressure barycenter coordinate is observed.

The role of the underbody flow as a function of the ground clearance is now investigated. Velocity profiles are then measured 2 mm behind the body using a classical hot wire probe, in the midplane $y = 0$ for different ground clearances C^*. They are all presented in Fig. 6 as z/C versus the velocity with a vertical shift for clarity. For large ground clearances, $C^* > 0.04$, velocity profiles are well established and present a relatively parabolic shape. The velocity fluctuations are maximum [Fig. 8(b)] on the top side of the profiles which corresponds to the free mixing layer and on the bottom side that corresponds to the boundary layer on the floor. For ground clearances smaller than $C^* < 0.04$, there is no established underbody flow and a transition with high velocity fluctuations is observed for $C^* = 0.021$.

To study the two stable solutions of the bifurcated states, we chose to explore the wake positions for the two yaw angles $\beta = -0.4^\circ$ in Fig. 7(a) and $\beta = +0.4^\circ$ in Fig. 7(b). The negative (respectively, positive) yaw angle allows exploration of the branch y^{*+}_b (respectively, y^{*-}_b) corresponding to the positive (respectively, negative) part of PDF(y^*_b). As can be seen, the system explores preferentially the y^{*+} branch near the bifurcation point which is evidence for an imperfect bifurcation. In addition, we never noticed any hysteretic effect by working with increasing or decreasing control parameters, which reinforces the supercritical character of the bifurcation. For both PDF branches, the position of the local maxima are extracted [plotted as white lines in Figs. 7(a) and 7(b)]. This technique of extraction will be repeated in the following to study the Reynolds number effect on the bifurcation diagram.

Figure 7(c) displays the maximum values of the profiles measured in Fig. 6. It is clear from these results that the

underbody flow is already well established, about U_0 at the pitchfork point of the bifurcation observed around $C^* \sim 0.075$. Hence, the large velocity fluctuations observed at $C^* = 0.021$ occurs at a too-small ground clearance to be associated with the instability threshold of the RSB states.

C. Bifurcation threshold with Reynolds number

Nine experiments with different Reynolds numbers have been conducted with exactly the same protocol as for the previous experiment. All of the bifurcation diagrams obtained by superimposing the branch y^{*+} and y^{*-} are shown in Fig. 8.

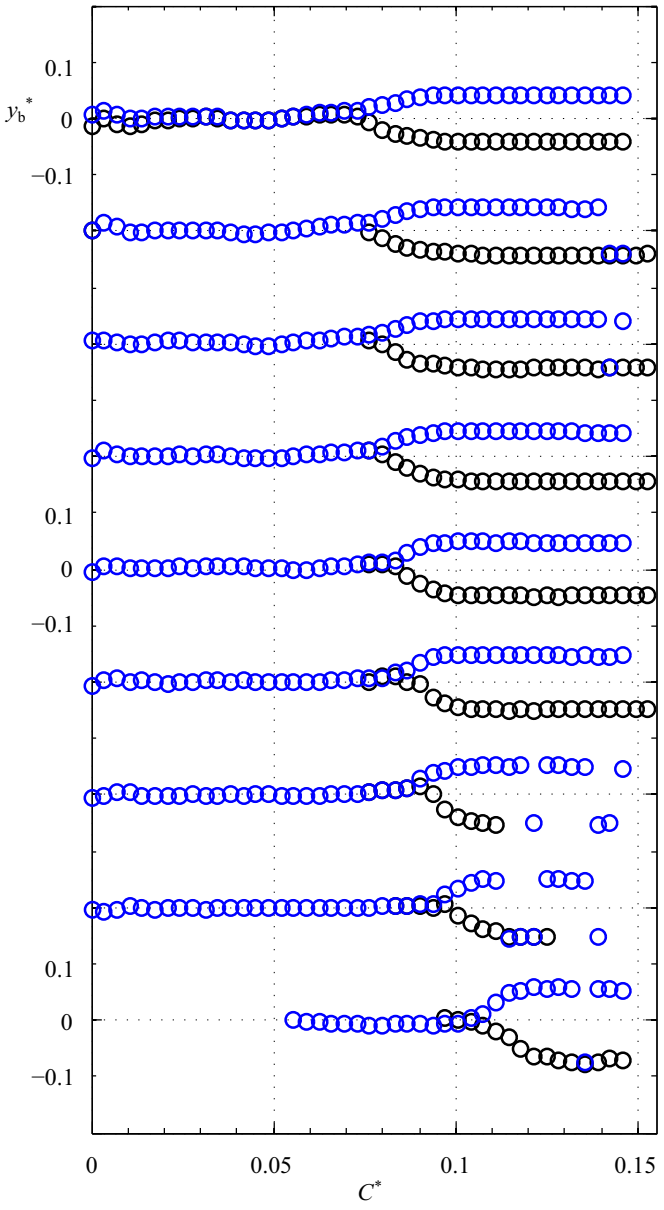

FIG. 8. (Color online) Bifurcation diagrams vs the ground clearance obtained with different Reynolds numbers from bottom to top: $\mathrm{Re} = 1.78 \times 10^4, 2.89 \times 10^4, 3.95 \times 10^4, 5.05 \times 10^4, 6.1 \times 10^4, 8.27 \times 10^4, 1.04 \times 10^5, 1.32 \times 10^5, 1.6 \times 10^5$. For each Reynolds number, the branches are extracted from the most probable position of the barycenter obtained from $\beta = -0.4^\circ$ (blue circles) and $\beta = +0.4^\circ$ (white circles) as in Figs. 7(a) and 7(b).

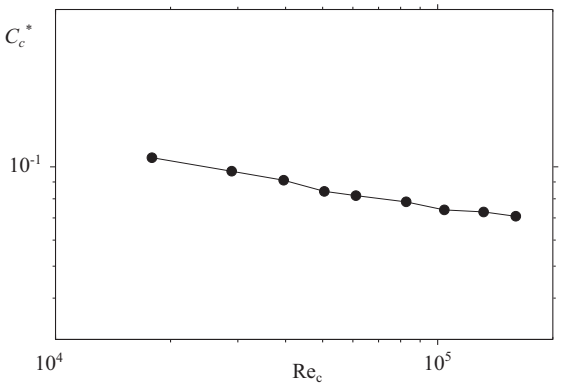

FIG. 9. Threshold of the bifurcation, critical ground clearance vs critical Reynolds number.

We can see clear imperfect pitchfork bifurcations due to some symmetry defects before and at the bifurcation point. As said above, these imperfections are likely to be explained by the free stream properties characterized in Fig. 2. The bifurcation point, defined as the crossing point between the two branches, appears to depend on the Reynolds number, and its dependency is shown in Fig. 9. The uncertainty about C_c^* is estimated to be ± 0.0025, reflecting the measurements displayed in Fig. 8(a).

The critical ground clearance C_c^* is a slow decreasing function of the critical Reynolds number Re_c, similar to the power law $\mathrm{Re}_c^{-1/6}$ in the range of our experiments.

D. Toward a stabilization using passive control

We now investigate the possibility for the existence of an unstable branch solution, corresponding to the prolongation of the symmetric state after the bifurcation point. The idea is to apply the passive control technique first introduced by Ref. [28] to stabilize the Kármán instability in the laminar wake of a circular cylinder. It has been shown for the present configuration in Ref. [24] to efficiently eliminate the bimodal behavior of the turbulent wake. It consists in a steady disturbance technique by introducing inside the recirculating bubble a vertical cylinder, having the same height as the body with a diameter $d^* = 0.083$. We placed the control cylinder at the best location obtained in Ref. [24], say, $y^* = 0$ and $x^* = 0.52$. Two thin rods, as depicted in Fig. 10(b), support the control cylinder. In order to characterize the effect of the control cylinder only, a bifurcation diagram has been performed with the body and the two thin rods as a function of the ground clearance. It is shown in Fig. 10(a). Because of the thickness of the rod under the body, the ground clearance is limited for low values to $C^* = 0.035$. The observed bifurcation, very similar to the one obtained without the rods (Fig. 7), attests from the neutrality of the supporting system. Furthermore, it has to be mentioned that the bifurcation in Fig. 10(a) is obtained for only one yaw angle. It has been especially adjusted in order to have the best equiprobable exploration of the two states at the largest ground clearance. In this condition, we see that both branches are randomly explored after the bifurcation point, leading to the bistable dynamics of the wake.

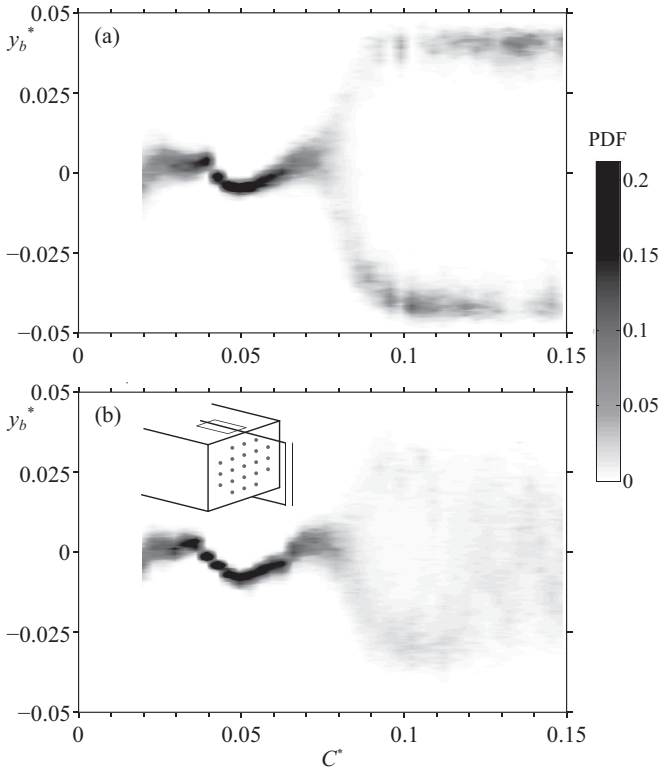

FIG. 10. Probability density functions, PDF(y_b^*), in gray levels for $U_0 = 30.58\ \mathrm{m\,s^{-1}}$ vs the ground clearance C^*, for (a) with the yaw angle $\beta = -0.4^\circ$ and (b) with a yaw angle $\beta = +0.4^\circ$. The white lines represent the most probable position and correspond in (a) (continuous line) to the stable branch y_b^{*+} and in (b) (dashed line) to the other stable branch y_b^{*-}.

When the control cylinder is placed between the two rods, the bifurcation diagram before the pitchfork point remains unaltered compared to that of the reference, while after the pitchfork point the two branches are replaced by a continuum of uniform density probability over values of $y^\star$ included within $y_b^{\star\pm}$, yet excluding $y_b^{\star\pm}$. At this point it is difficult to argue whether the system is actually stabilized since there is no most probable position around $y^* = 0$. However, the system is definitely no longer bimodal. This simple experiment is promising since passive control can be considerably improved using active control. We are confident that the latter will be the good strategy to stabilize the wake.

Although the suppression of the lateral force can be achieved by stabilizing the flow, it remains interesting to look at the effect of a stabilization on the base suction and hence the drag. The base suction as defined in Eq. (3) is shown in Fig. 11. The dashed line refers to the reference case; it displays large variations of the base suction coefficient due to the development of the underbody flow as already described in Ref. [20] and characterized in Fig. 6. However, the abrupt change observed for $C^* \sim 0.09$ is clearly ascribed to the pitchfork point, indicating that the presence of the RSB modes are creating additional base suction and then drag. By stabilizing the wake, one would expect the base suction coefficient to decrease in the continuity of its evolution before

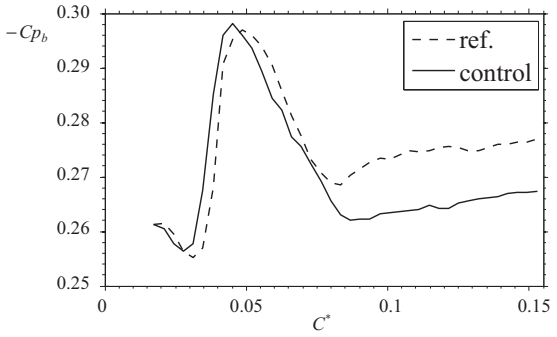

FIG. 11. Base pressure suction vs the ground clearance for (dashed line) the reference case of Fig. 10(a) and for (continuous line) the controlled case of Fig. 10(b).

the pitchfork point. It is actually what is observed when the control cylinder is added, the base suction follows the same variations as for the reference case. After the instability threshold, a significant reduction is observed. This passive control experiment is encouraging as a new strategy for drag reduction of three-dimensional (3D) turbulent wakes.

E. Flow visualizations

We turn now to an illustrative experiment of flow visualization realized in a water tunnel. The model is a 1:2.66 scale of the one used above. The test section of the tunnel is 80 × 150 mm and the flow speed 6 $\mathrm{m\,s^{-1}}$. The Reynolds number is 216 000, and the ground clearance is set to $C^* = 0.1$. The yaw angle is accurately adjusted to obtain the bistable dynamics of the two RSB states. We present in Fig. 12 some pictures extracted from a long-time movie [29] showing the random switching between the y_b^+ stable solution shown in Fig. 12(a) and the y_b^- stable solution shown in Fig. 12(b). The two wake states present a mirror symmetry, with an intense circular recirculation clearly visible on the right-hand side in Fig. 12(a) and symmetrically on the left-hand side in Fig. 12(b). The low-pressure barycenter position is on the same side as this intense recirculation. These flow visualizations are in total agreement with the velocity field measurements of the RSB modes in Ref. [19]. When a vertical control cylinder is added as in Sec. III D, a symmetric wake is observed without any intense recirculations.

IV. CONCLUSIVE REMARKS

The wake of a square-back body at the proximity of a ground wall undergoes a pitchfork bifurcation in the turbulent regime from a symmetric turbulent wake toward two asymmetric turbulent wakes. The phase diagram in Fig. 9 indicates that the critical ground clearance is a slow decreasing function of the critical Reynolds number. Thus, the bifurcation is also observable for a given ground clearance as the Reynolds number is increased. The smaller the ground clearance the larger the Reynolds number for the transition. At the threshold of the instability (pitchfork point), the underbody flow magnitude is approximately U_0 [see Fig. 7(c)], indicating that the bifurcation is not related to a flow transition in the

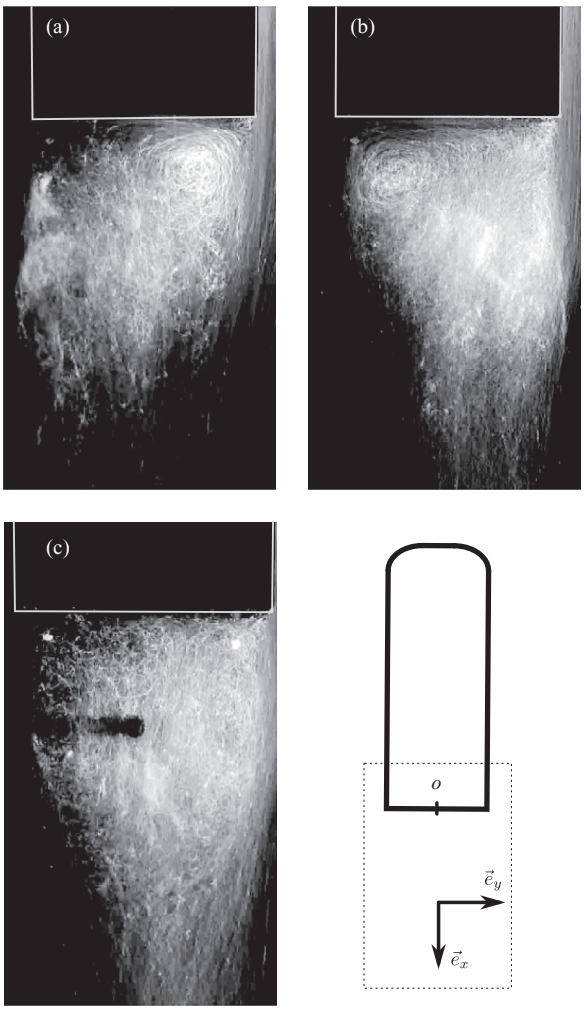

FIG. 12. Flow visualization performed in a water tunnel using bubbles appearing white against a black background. The flow Reynolds number is Re = 216 000 at a ground clearance $C^* = 0.1$. The drawing shows the visualization area depicted by a dashed rectangle at the rear of the Ahmed body. The obturation time of the camera is $\tau^* = 3$, say, 3 times larger than the convective time H/U_0, and captures the dynamics at this time scale. In (a), the RSB mode of the branch y_b^+ and in (b) its mirror counterpart, the RSB mode of the branch y_b^-. In (c), the wake controlled with a vertical control cylinder (diameter $d^* = 0.107$).

ground clearance. Following the idea of Grandemange *et al.* [20], the crucial ingredient for the symmetry breaking is the ratio between the separating distances of the vortex sheets produced by the separation at the rectangular base (it is also the result of the stability analysis by Marquet and Larsson [22] for a rectangular plate facing a uniform flow in the laminar regime). The inviscid condition at the ground wall, which can be justified for large Re flow, is equivalent to a mirror flow. In the absence of the underbody flow, the top vortex sheet emerging from the square-back body is then facing its symmetric counterpart at a distance that is double the body height, $2H$. In the case of an underbody flow, a second vortex sheet emerges from the bottom trailing edge of the body and the separating distance with the top vortex sheet is now H. For the primary case, the aspect ratio is twice the second case and does not allow the symmetry-breaking instability at the given width W of the base [20]. Hence the large Reynolds number bifurcation appears to be related to a stabilizing geometrical parameter. One may wonder if an equivalent explanation can be tested on the transition obtained with the von Kármán swirling flow geometry.

There are some interesting applications for flow control of 3D turbulent wakes, for instance, the pioneering technique of Strykowski and Sreenivasan [30] to stabilize the periodic laminar von Kármán instability toward the steady state is also efficient to stabilize the turbulent RSB mode toward a symmetric wake mode. In addition to the flow studied here, it is known that the turbulent wake of axisymmetric bodies develops symmetry-breaking modes as well [25,31]. Thus the stabilization toward the symmetric unstable mode might be a relevant strategy for drag and lateral force reduction in many applications with potentially a low energetic cost and offers promising future development.

ACKNOWLEDGMENTS

The authors are grateful to Romain Monchaux for useful discussions about the von Kármán swirling flow and thankful to John Wrightson for his critical reading of the manuscript. This work benefited from the financial support of LaSIPS in the framework of the TURBFORK project.

[1] U. Frisch, *Turbulence* (Cambridge University Press, Cambridge, 1996).
[2] H. Schlichting and K. Gersten, *Boundary Layer Theory* (Springer-Verlag, Berlin, 2000).
[3] P. Bearman, J. Fluid Mech. **37**, 577 (1969).
[4] E. Achenbach and E. Heinecke, J. Fluid Mech. **109**, 239 (1981).
[5] G. Schewe, J. Fluid Mech. **133**, 265 (1983).
[6] G. Schewe, J. Fluid Mech. **172**, 33 (1986).
[7] C. Farell and J. Blessmann, J. Fluid Mech. **136**, 375 (1983).
[8] J. J. Miau, H. W. Tsai, Y. J. Lin, J. K. Tu, C. H. Fang, and M. C. Chen, Exp. Fluids **51**, 949 (2011).
[9] Y.-J. Lin, J.-J. Miau, J.-K. Tu, and H.-W. Tsai, AIAA J. **49**, 1857 (2011).
[10] O. Cadot, A. Desai, S. Mittal, S. Saxena, and B. Chandra, Phys. Fluids **27**, 014101 (2015).
[11] F. Ravelet, L. Marie, A. Chiffaudel, and F. Daviaud, Phys. Rev. Lett. **93**, 164501 (2004).
[12] A. de la Torre and J. Burguete, Phys. Rev. Lett. **99**, 054101 (2007).
[13] F. Ravelet, F. Chiffaudel, and A. Daviaud, J. Fluids Mech. **601**, 339 (2008).
[14] P.-P. Cortet, A. Chiffaudel, F. Daviaud, and B. Dubrulle, Phys. Rev. Lett. **105**, 214501 (2010).

[15] P.-P. Cortet, E. Herbert, A. Chiffaudel, F. Daviaud, B. Dubrulle, and V. Padilla, J. Stat. Mech. Theor. Exp. (2011) P07012.
[16] C. Nore, L. Tuckerman, O. Daube, and S. Xin, J. Fluid Mech. **477**, 51 (2003).
[17] C. Nore, L. Witkowski, E. Foucault, J. Pecheux, O. Daube, and P. Le Quere, Phys. Fluids **18**, 054102 (2006).
[18] M. Grandemange, O. Cadot, and M. Gohlke, Phys. Rev. E **86**, 035302(R) (2012).
[19] M. Grandemange, M. Gohlke, and O. Cadot, J. Fluid Mech. **722**, 51 (2013).
[20] M. Grandemange, M. Gohlke, and O. Cadot, Phys. Fluids **25**, 095103 (2013).
[21] B. Pier, J. Fluid Mech. **603**, 39 (2008).
[22] O. Marquet and M. Larsson, Eur. J. Mech. B. **49**, 400 (2014).
[23] S. Ahmed, G. Ramm, and G. Faitin, SAE Technical Paper Series 840300 (1984).
[24] M. Grandemange, M. Gohlke, and O. Cadot, J. Fluid Mech. **752**, 439 (2014).
[25] G. Rigas, A. Oxlade, A. Morgans, and J. Morrison, J. Fluid Mech. **755**, 159 (2014).
[26] A. Roshko, J. Wind Eng. Ind. Aerod. **49**, 79 (1993).
[27] C. Apelt and G. West, J. Fluid Mech. **71**, 145 (1975).
[28] P. Strykowski and K. Sreenivasan, J. Fluid Mech. **218**, 71 (1990).
[29] See Supplemental Material at http://link.aps.org/supplemental/10.1103/PhysRevE.91.063005 for movies of a symmetric and a bistable wake.
[30] P. J. Strykowski and K. R. Sreenivasan, in *AIAA Shear Flow Control Conference, Boulder, Colorado, 1985* (AIAA, Reston, VA, 1985).
[31] M. Grandemange, M. Gohlke, and O. Cadot, Exp. Fluids **55**, 1 (2014).